Publication Year	2017
Acceptance in OA	2020-11-19T08:43:33Z
Title	Precise strong lensing mass profile of the CLASH galaxy cluster MACS 2129
Authors	Monna, A., Seitz, S., Balestra, I., Rosati, P., Grillo, C., Halkola, A., Suyu, S. H., Coe, D., Caminha, G. B., Frye, B., Koekemoer, A., MERCURIO, AMATA, NONINO, Mario, Postman, M., Zitrin, A.
Publisher's version (DOI)	10.1093/mnras/stx015
Handle	http://hdl.handle.net/20.500.12386/28435
Journal	MONTHLY NOTICES OF THE ROYAL ASTRONOMICAL SOCIETY
Volume	466

Monthly Notices of the ROYAL ASTRONOMICAL SOCIETY

MNRAS **466,** 4094–4106 (2017)
Advance Access publication 2017 January 7

doi:10.1093/mnras/stx015

Precise strong lensing mass profile of the CLASH galaxy cluster MACS 2129

A. Monna,[1,2★] S. Seitz,[1,2] I. Balestra,[1,3] P. Rosati,[4] C. Grillo,[5,6] A. Halkola,[7] S. H. Suyu,[8,9,10] D. Coe,[11] G. B. Caminha,[4] B. Frye,[12] A. Koekemoer,[11] A. Mercurio,[13] M. Nonino,[3] M. Postman[11] and A. Zitrin[14,15†]

[1] *University Observatory Munich, Scheinerstrasse 1, D-81679 Munich, Germany*
[2] *Max Planck Institute for Extraterrestrial Physics, Giessenbachstrasse, D-85748 Garching, Germany*
[3] *INAF, Osservatorio Astronomico di Trieste, via G. B. Tiepolo 11, I-34131 Trieste, Italy*
[4] *Dipartimento di Fisica e Scienze della Terra, Universitá di Ferrara, via Saragat 1, I-44122 Ferrara, Italy*
[5] *Dipartimento di Fisica, Università degli Studi di Milano, via Celoria 16, I-20133 Milano, Italy*
[6] *Dark Cosmology Centre, Niels Bohr Institute, University of Copenhagen, Juliane Maries Vej 30, DK-2100 Copenhagen, Denmark*
[7] *Institute of Medical Engineering, University of Lübeck, Ratzeburger Allee 160, D-23562 Lübeck, Germany*
[8] *Max-Planck-Institut für Astrophysik, Karl-Schwarzschild-Str. 1, D-85741 Garching, Germany*
[9] *Institute of Astronomy and Astrophysics, Academia Sinica, PO Box 23-141, Taipei 10617, Taiwan*
[10] *Physik-Department, Technische Universität München, James-Franck-Straße 1, D-85748 Garching, Germany*
[11] *Space Telescope Science Institute, 3700 San Martin Drive, Baltimore, MD 21208, USA*
[12] *Department of Astronomy/Steward Observatory, University of Arizona, 933 North Cherry Avenue, Tucson, AZ 85721, USA*
[13] *INAF, Osservatorio Astronomico di Capodimonte, Via Moiariello 16, I-80131 Napoli, Italy*
[14] *Cahill Center for Astronomy and Astrophysics, California Institute of Technology, MC 249-17, Pasadena, CA 91125, USA*
[15] *Physics Department, Ben-Gurion University of the Negev, PO Box 653, Beér-Sheva 84105, Israel*

Accepted 2017 January 4. Received 2017 January 4; in original form 2016 May 27

ABSTRACT

We present a detailed strong lensing (SL) mass reconstruction of the core of the galaxy cluster MACS J2129.4−0741 ($z_{\rm cl} = 0.589$) obtained by combining high-resolution *Hubble Space Telescope* photometry from the CLASH (Cluster Lensing And Supernovae survey with Hubble) survey with new spectroscopic observations from the CLASH-VLT (Very Large Telescope) survey. A background bright red passive galaxy at $z_{\rm sp} = 1.36$, sextuply lensed in the cluster core, has four radial lensed images located over the three central cluster members. Further 19 background lensed galaxies are spectroscopically confirmed by our VLT survey, including 3 additional multiple systems. A total of 31 multiple images are used in the lensing analysis. This allows us to trace with high precision the total mass profile of the cluster in its very inner region ($R < 100$ kpc). Our final lensing mass model reproduces the multiple images systems identified in the cluster core with high accuracy of 0.4 arcsec. This translates to a high-precision mass reconstruction of MACS 2129, which is constrained at a level of 2 per cent. The cluster has Einstein parameter $\Theta_{\rm E} = (29 \pm 4)$ arcsec and a projected total mass of $M_{\rm tot}(<\Theta_{\rm E}) = (1.35 \pm 0.03) \times 10^{14}\,{\rm M}_{\odot}$ within such radius. Together with the cluster mass profile, we provide here also the complete spectroscopic data set for the cluster members and lensed images measured with VLT/Visible Multi-Object Spectrograph within the CLASH-VLT survey.

Key words: gravitational lensing: strong – galaxies: clusters: general – dark matter.

1 INTRODUCTION

Clusters of galaxies are the largest gravitationally bounded structures in the Universe and play a fundamental role in testing cosmological models, investigating the formation and growth of structures of the Universe and properties of dark matter (DM). The combination of different independent techniques [stellar kinematics in the brightest cluster galaxy (BCG), X-ray, weak and strong lensing (SL), stellar kinematics, etc.] allows one to robustly constrain the DM density profile of galaxy clusters from the inner region up to large radial distances (∼5 Mpc; see Sand, Treu & Ellis 2002; Sand et al. 2004; Newman et al. 2009, 2011; Umetsu et al. 2012, 2016;

★E-mail: anna.monna@gmail.com
† Hubble Fellow.

© 2017 The Authors
Published by Oxford University Press on behalf of the Royal Astronomical Society

Downloaded from https://academic.oup.com/mnras/article/466/4/4094/2869856 by guest on 19 November 2020

Biviano et al. 2013; Balestra et al. 2016). Gravitational lensing offers a unique technique to investigate the mass distribution of galaxy clusters, since it is generated by the total mass of the lens, i.e. both the baryonic and DM components. In the strong lensing regime, when giant arcs and multiple images of background sources are generated, the mass distribution of the inner region of galaxy clusters can be reconstructed in great detail (e.g. see Eichner et al. 2013; Grillo et al. 2015; Monna et al. 2015). In this context, the Cluster Lensing And Supernovae survey with Hubble (CLASH; Postman et al. 2012) and the CLASH-VLT (Very Large Telescope) survey provide high-resolution photometry and spectroscopic data set to measure cluster mass profiles by combining strong and weak lensing analyses (see Coe et al. 2012; Umetsu et al. 2012; Medezinski et al. 2013). In particular, the total mass profile of inner regions ($R < 100$–200 kpc) of galaxy clusters can be derived with extremely high precision of few percentage using deep high-resolution *Hubble Space Telescope* (*HST*) photometry, as that collected by the CLASH and the deeper Hubble Frontier Fields (PI: J. Lotz) surveys (e.g. see Grillo et al. 2015; Jauzac et al. 2015).

In this paper, we present the strong lensing reconstruction of the core of the galaxy cluster MACS J2129.4−0741 (Ebeling et al. 2007, hereafter MACS 2129) using the high-resolution photometry from CLASH and new spectroscopy from the CLASH-VLT survey. This is a massive galaxy cluster ($M_{2500} = 4.7 \pm 1.7 \times 10^{14} h_{70}^{-1}\,\mathrm{M}_{\odot}$; Donahue et al. 2014), selected within the CLASH survey for its lensing strength. A peculiar bright red galaxy is sextuply lensed in its core, and the deflection of this multiple system is strongly affected by the gravitational action of the central galaxies. Six further multiple images systems are identified in the cluster core. These allow us to put strong constraints on the mass distribution in the innermost region of the cluster. Zitrin et al. (2011) present a first strong lensing model of the cluster, which is subsequently refined using the CLASH photometry in Zitrin et al. (2015), reproducing the multiple images with rms of ∼2 arcsec. Here we perform a more detailed analysis of the cluster core and take advantage of the new CLASH-VLT spectroscopic data to trace the cluster mass distribution with higher accuracy.

The paper is organized as follows. In Section 2, we present the photometric and spectroscopic data set. In Section 3, we introduce the cluster mass components and the lensed systems used in the analysis. In Section 4, we describe the performed lensing analysis and in Section 5 we provide and discuss the results. Summary and conclusions are given in Section 6. Finally in Appendix A, we summarize the CLASH spectroscopy for the background sources and cluster members, and provide the 2D spectra and spectral energy distribution (SED) fit of the multiple images used in the lensing analysis.

Throughout the paper, we assume a cosmological model with Hubble constant $H_0 = 70$ km s^{-1} Mpc^{-1}, and density parameters $\Omega_{\mathrm{m}} = 0.3$ and $\Omega_{\Lambda} = 0.7$. Magnitudes are given in the AB system. At the redshift of the cluster ($z_{\mathrm{cl}} = 0.589$), 1 arcsec corresponds to 6.63 kpc.

2 PHOTOMETRIC AND SPECTROSCOPIC DATA SET

2.1 *HST* photometry

MACS 2129 was observed between 2011 May and August as part of the CLASH survey with the *HST* Advanced Camera for Surveys (ACS) and the *HST* Wide Field Camera 3 (WFC3) UVIS and IR cameras. These observations provide high-resolution photometry in 16 filters covering the UV, optical and NIR range. In addition, photometry in the ACS/WFC/*F*555*W* filter is also available from the public *HST* archive. The photometric data set (available at http://archive.stsci.edu/prepds/clash, see Postman et al. 2012) is composed of *HST* mosaic drizzled 65 mas pixel^{-1} images generated with the `Mosaicdrizzle` pipeline (see Koekemoer et al. 2011). These cover a field of view (FOV) of ∼3.5 arcmin × 3.5 arcmin in the ACS images and ∼2 arcmin × 2 arcmin in the WFC3IR images. Fig. 1 shows a colour composite image of the cluster core, created using the CLASH *HST* data set. In Table 1, we list the complete filter list of our photometric data set with the respective total exposure time and 5σ detection limit.

Table 1. Photometric data set summary for MACS 2129. Column 1: filters; column 2: total observation time in seconds; column 3: *HST* instrument; column 4: the 5σ magnitude depth within 0.6 arcsec.

Filter	Total time (s)	Instrument	5σ depth
*F*225*W*	6934	WFC3/UVIS	25.37
*F*275*W*	7243	WFC3/UVIS	25.42
*F*336*W*	4580	WFC3/UVIS	25.78
*F*390*W*	4563	WFC3/UVIS	26.47
*F*435*W*	3728	ACS/WFC	26.22
*F*475*W*	4040	ACS/WFC	26.64
*F*555*W*	8880	ACS/WFC	26.97
*F*606*W*	3728	ACS/WFC	26.86
*F*625*W*	3846	ACS/WFC	26.37
*F*775*W*	4048	ACS/WFC	26.24
*F*814*W*	13396	ACS/WFC	27.14
*F*850*LP*	7808	ACS/WFC	25.91
*F*105*W*	1006	WFC3/IR	26.21
*F*110*W*	1409	WFC3/IR	26.72
*F*125*W*	1409	WFC3/IR	26.41
*F*140*W*	2312	WFC3/IR	26.87
*F*160*W*	3620	WFC3/IR	26.66

Using these data, we generate a multi-band photometric catalogue of fluxes extracted within 0.6 arcsec (9 pixels) diameter aperture, using SExtractor 2.8.6 (Bertin & Arnouts 1996) in dual image mode. As detection image we use the weighted sum of all the WFC3IR images.

2.2 VLT spectroscopy

MACS 2129 was observed with the Visible Multi-Object Spectrograph (VIMOS; Le Fèvre et al. 2003) at ESO VLT as a part of the CLASH-VLT ESO Program 186.A-0798 (PI: P. Rosati; see Rosati et al. 2014). The cluster is partially obscured in the north-east side by a Galactic cirrus; thus, only the central and south-western portions of the cluster were targeted by our VIMOS observations, covering a field of 16 arcmin × 18 arcmin. Only two 4h-pointings were performed, one using the low-resolution blue grism (covering the spectral range of 3700–6700 Å with a resolution of 180) and one using the medium-resolution (MR) red grism (which covers the 4800–10 000 Å with a resolution of 580). The spectra were reduced with the VIMOS Interactive Pipeline and Graphical Interface (vipgi; Scodeggio et al. 2005) and redshifts were measured following the procedure described in Balestra et al. (2016). A quality flag (QF) is assigned to each spectroscopic redshift depending on if it is 'secure' (QF = 3), 'likely' (QF = 2), 'insecure' (QF = 1) or if it is based on a strong emission line (QF = 9). With a number of slits significantly reduced (∼1/10) compared to other clusters observed in the CLASH-VLT campaign, we obtained a total of 281 redshifts, including 48 cluster members and 19 lensed sources. In the core of

Downloaded from https://academic.oup.com/mnras/article/466/4/4094/2869856 by guest on 19 November 2020

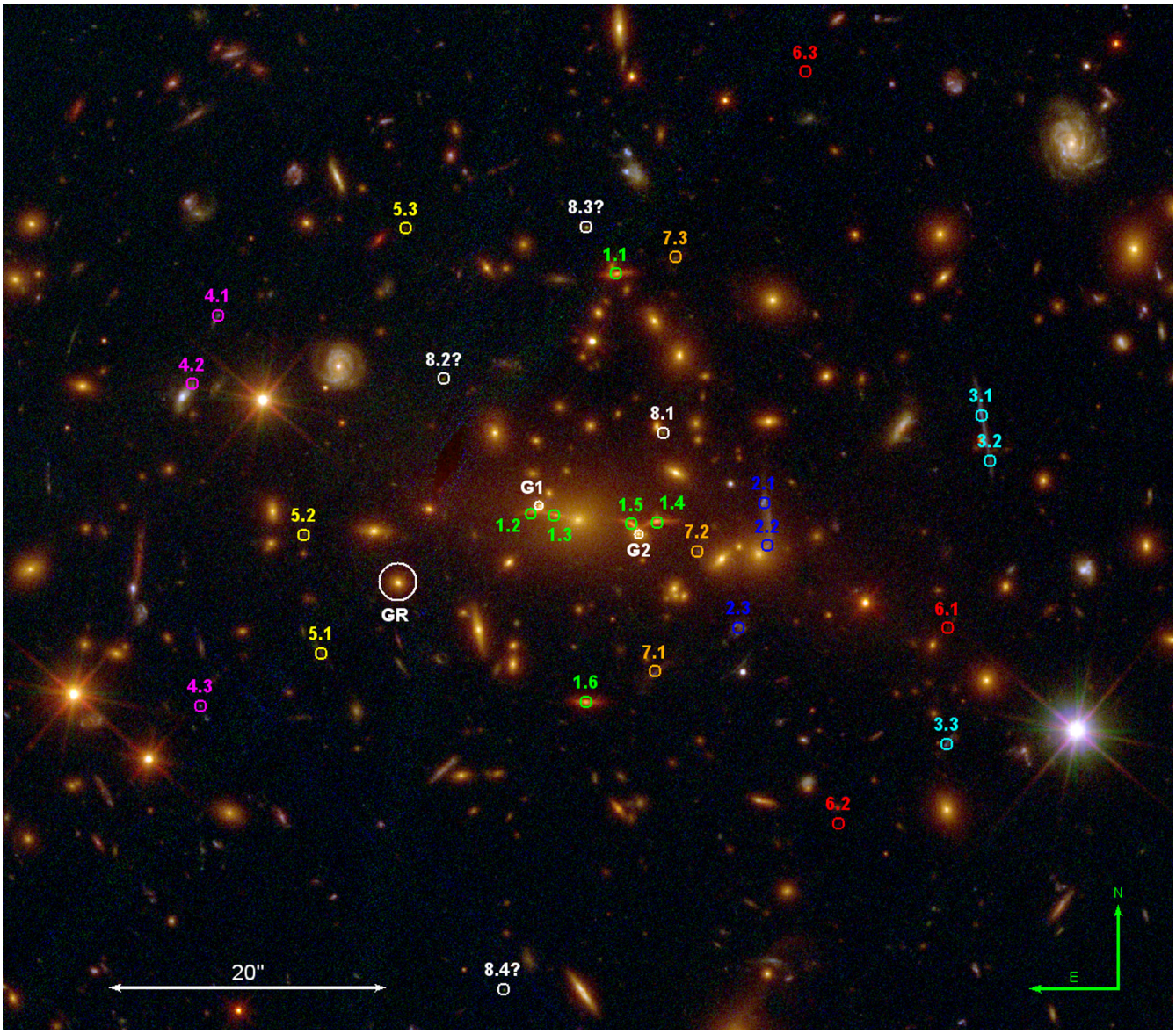

Figure 1. Colour composite image of the core of MACS 2129, generated using the CLASH *HST* data set: blue = $F435W+F475W$; green = $F555W+F606W+F625+F775W+F814W+F850LP$; red = $F105W+F110W+F125W+F140W+F160W$. We label with different colours and numbers the seven multiple images systems used in the SL analysis. All systems have spectroscopic measurements except systems 5 and 7. System 8 is a candidate quadruply lensed source. Image 8.1 was serendipitously discovered within our CLASH-VLT survey and has redshift $z_{sp} = 4.4$. We selected three candidate counter images based on photometry, which are labelled as 8.2, 8.3 and 8.4. We also label the galaxy GR used as reference for the galaxy luminosity scaling relation and the two cluster members G1 and G2 that are individually optimized in our model.

the cluster ($R < 1.5$ arcmin), we have secured redshifts for 4 cluster members, 4 multiple images systems and 15 additional lensed background sources. In Appendix A, we provide the complete list of spectroscopic redshifts of cluster members and lensing features with their respective QF (see Tables A1 and A2).

We also collected additional spectroscopic data available from the literature (Stern et al. 2010) that provide spectroscopic measurements of six further cluster members in the cluster core, observed with the Low-Resolution Imaging Spectrometer (LRIS) instrument on the Keck I telescope. Recently, new spectroscopic measurements for cluster members and lensing features of MACS 2129 have been released from the Grism Lens-Amplified Survey from Space (Treu et al. 2015). However, it provides no additional cluster member with robust z_{sp} measurement to our galaxy sample.

3 STRONG LENSING INGREDIENTS

We perform the strong lensing analysis in the core of MACS 2129, using the parametric mass modelling software 'Gravitational Lensing Efficient Explorer', developed by S. H. Suyu and A. Halkola (Suyu & Halkola 2010; Suyu et al. 2012). We adopt parametric mass profiles to describe the smooth large-scale cluster dark halo (DH) and the cluster members. The positions of the observed multiple images are used as constraints to estimate the mass profile parameters. Through a simulated annealing minimization in the image plane, we derive the best-fitting model that reproduces the observed images. Then we perform a Monte Carlo Markov chain (MCMC) sampling to find the most probable parameters and uncertainties for the cluster mass components.

Downloaded from https://academic.oup.com/mnras/article/466/4/4094/2869856 by guest on 19 November 2020

Table 2. List of the spectroscopically confirmed cluster members in the core of MACS 2129. Column 1: ID; Columns 2 and 3: RA and Dec. in degrees; column 4: auto magnitude extracted with SExtractor in the $F814W$ filter; column 5: spectroscopic redshift.

ID	RA	Dec.	$F814W_{\rm auto}$	z
873	322.357 12	−7.689 09	22.19 ± 0.01	0.583[a]
945	322.354 95	−7.691 78	20.16 ± 0.01	0.596[a]
1298	322.350 95	−7.697 15	20.92 ± 0.01	0.593[a]
1747	322.353 24	−7.707 95	21.15 ± 0.01	0.590[a]
BCG	322.3588	−7.691 05	19.42 ± 0.01	0.589[b]
884	322.342 65	−7.689 53	20.47 ± 0.01	0.590[b]
947	322.355 74	−7.691 88	20.41 ± 0.01	0.586[b]
984	322.3631	−7.691 29	20.92 ± 0.01	0.579[b]
1167	322.350 13	−7.694 43	21.10 ± 0.01	0.586[b]
1676	322.3504	−7.706 33	19.68 ± 0.01	0.596[b]

[a]Redshift measurement from CLASH-VLT survey.
[b]Redshift measurement from Stern et al. (2010).

3.1 Cluster DM halo

The large-scale smooth DH of the cluster is described through a pseudo-isothermal elliptical mass distribution (PIEMD) profile (Kassiola & Kovner 1993), with projected surface mass density given by

$$\Sigma(R) = \frac{\sigma^2}{2G}\left(r_c^2 + R^2\right)^{-0.5}, \quad (1)$$

where σ is the halo velocity dispersion and r_c is the core radius. The projected radius R is given by $R^2 = x^2/(1+e)^2 + y^2/(1-e)^2$, where $e = (1 - b/a)/(1 + b/a)$ is the halo ellipticity and b/a is the halo axial ratio. For ($b/a \to 1$, $r_c \to 0$), the asymptotic Einstein radius θ_E is given by

$$\theta_E = 4\pi\left(\frac{\sigma}{c}\right)^2 \frac{D_{ds}}{D_s} = \Theta_E \frac{D_{ds}}{D_s}, \quad (2)$$

where D_s is the source distance and D_{ds} is the distance between the lens and the source. In equation (2), we introduce the Einstein parameter Θ_E, which is the Einstein ring when the ratio D_{ds}/D_s is 1. In our analysis, the amplitude of the DH mass component is described through the Einstein parameter Θ_E, which is optimized in the range [5 arcsec, 45 arcsec]. The core radius r_c is optimized within [0 arcsec, 25 arcsec], while position angle PA and axial ratio vary within [−90°, 90°] and [0, 1], respectively. The position of the DH centre is optimized within ±3 arcsec around the central brightest cluster member (BCG). We adopt flat priors on all the DH parameters.

3.2 Cluster members

In addition to the 10 spectroscopic members (see Table 2), we select further cluster members in the core of the cluster ($R < 1.5$ arcmin) using the CLASH photometry. These are bright ($F814W_{\rm auto} < 24$) galaxies that lie on the cluster red sequence ($F625W - F814W \leq 1 \pm 0.3$), see Fig. 2. In addition, we require that these candidate cluster members have photometric redshift $z_{\rm ph}$ within $z_{\rm cl} \pm \Delta z$, with $\Delta z = 0.04(1 + z_{\rm cl})$. Photometric redshifts are computed based on the CLASH photometry using the SED fitting code LEPHARE[1] (Arnouts et al. 1999; Ilbert et al. 2006). To estimate photometric redshifts, we use galaxy SED templates from the COSMOS (Ilbert et al. 2009) template set.

[1] http://www.cfht.hawaii.edu/~arnouts/lephare.html

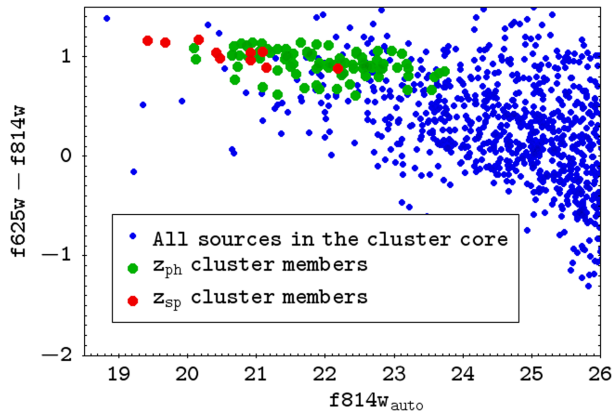

Figure 2. Colour–magnitude diagram for sources extracted in the WFC3IR FOV of the cluster MACS 2129 at $z = 0.589$. We plot the colour from the aperture magnitudes $F625W$ and $F814W$, versus the SExtractor mag_best in the $F814W$ filter. Blue circles are all the sources extracted in the WFC3IR FOV; red circles are the spectroscopically confirmed cluster members; green circles are cluster member candidates with $z_{\rm ph} \in [0.52, 0.65]$ and $F814W$_mag_best < 24.

To account for the interstellar medium extinction, we apply the Calzetti extinction law (Calzetti et al. 2000) to the starburst templates, and the Small Magellanic Cloud Prevot law (Prevot et al. 1984) to the Sc and Sd templates.

We select 83 bright cluster member candidates in the cluster core based on the photometry. Two further galaxies are included in the sample after visual inspection, which have bluer colour ($F625W - F814W \sim 0.6$) due to photometric contamination by nearby blue sources. We have a total of 85 candidate cluster members that add to the 10 spectroscopically confirmed ones.

These 95 galaxies are included in the cluster SL mass model and are described with dual pseudo-isothermal elliptical profiles (dPIE; Elíasdóttir et al. 2007). The projected surface mass density for this profile is

$$\Sigma(R) = \frac{\sigma^2}{2GR}\frac{r_{\rm tr}^2}{r_{\rm tr}^2 - r_c^2}\left(\frac{1}{\sqrt{1 + r_c^2/R^2}} - \frac{1}{\sqrt{1 + r_{\rm tr}^2/R^2}}\right), \quad (3)$$

where $R^2 = x^2/(1+e)^2 + y^2/(1-e)^2$ as for the PIEMD mass profile, r_c is the core radius and $r_{\rm tr}$ is the so-called truncation radius that marks the region where the density slope changes from $\rho \propto r^{-2}$ to $\rho \propto r^{-4}$. The total mass for this profile is given by

$$M_{\rm tot} = \frac{\pi\sigma^2}{G}\frac{r_{\rm tr}^2}{r_{\rm tr} + r_c}. \quad (4)$$

We use vanishing core radii for the galaxies; thus, for each galaxy mass profile, we have two free parameters, i.e. the velocity dispersion σ and the truncation radius $r_{\rm tr}$.

We adopt as reference galaxy (GR) one of the candidate cluster members, and then derive the velocity dispersion and size of all the other cluster members through the following luminosity scaling relations, according to the Faber–Jackson and the Fundamental Plane relations:

$$\sigma = \sigma_{\rm GR}\left(\frac{L}{L_{\rm GR}}\right)^{\delta} \quad (5)$$

$$r_{\rm tr} = r_{\rm tr,GR}\left(\frac{L}{L_{\rm GR}}\right)^{\alpha} = r_{\rm tr,GR}\left(\frac{\sigma}{\sigma_{\rm GR}}\right)^{\frac{\alpha}{\delta}}. \quad (6)$$

Downloaded from https://academic.oup.com/mnras/article/466/4/4094/2869856 by guest on 19 November 2020

Following our previous work, we adopt as exponent of the scaling relations $\delta = 0.3$ and $\alpha = 0.4$, assuming a constant mass-to-light ratio. See Eichner et al. (2013) and Monna et al. (2015) for a detailed derivation of these values.

The reference galaxy GR (RA = 322.3626, Dec. = −7.692 38 deg, see Fig. 1) is a cluster member with magnitude $F814W_{\rm auto} = 21.3$ and axial ratio $b/a = 0.95$, which lies ∼14 arcsec from the BCG. The velocity dispersion and truncation radius of GR are optimized with flat priors within the ranges of [100,300] km s^{-1} and [1,100] kpc, respectively. The mass parameters σ and $r_{\rm tr}$ for all the other cluster members are then derived through the previous scaling relation.

The three central galaxies (the BCG and the two galaxies G1 and G2, lying on its sides, see Fig. 1) clearly affect the distortion of the radial multiple images of system 1; thus, we individually optimized their parameters through the analysis.

The truncation radii for these galaxies vary within [1,100] kpc and the velocity dispersions are optimized in [100,300] km s^{-1}, except for the BCG for which we use a larger range of [100,410] km s^{-1}. In addition, also their axial ratio b/a and position angle PA are optimized, using the value extracted from the $F814W$ image with Gaussian priors.

For all the other galaxies, b/a and PA are fixed to the value extracted with SExtractor in the filter $F814W$.

3.3 Lensed images

Eight systems of multiple images are clearly identified in the *HST* images of MACS 2129, see Fig. 1. Seven of these were presented in Zitrin et al. (2015, systems 1 to 7), while system 8 was serendipitously discovered as a $z_{\rm sp} = 4.4$ lensed source in the cluster core by our VLT observations. Within the CLASH-VLT survey, we targeted 21 lensed sources, including some belonging to the multiple images systems from Zitrin et al. (2015), which were bright enough for VIMOS follow-up. In Table A1 in Appendix A, we list the redshift measurement for all the lensed features: 10 objects have secure redshift measurement (QF = 3), nine sources have likely redshift estimate (QF = 2) and for two objects the $z_{\rm sp}$ are based on a strong emission line (QF = 9). We obtain spectroscopic measurement for five systems of multiple images (systems 1 to 4 and system 8). In addition, system 6 has been spectroscopically confirmed and analysed in detail in Huang et al. (2016). These spectroscopic measurements will be used as constraints in our strong lensing analysis. Two further systems of multiple images are used in the SL modelling (systems 5 and 7): these are identified by Zitrin et al. (2015) and have no spectroscopic measurement. The photometric redshifts of the multiple images associated with these systems are derived using the CLASH[2] photometry with the SED fitting code Bayesian Photometric Redshift, BPZ (see Table A1 and Fig. A3). In the lensing analysis, the mean $z_{\rm ph}$ for each system is used as the starting value for the source redshift z_s, and it is optimized with Gaussian prior using as width the 68 per cent uncertainties on the photometric redshift estimates.

In the following, we give a short description of each lensed system.

System 1. A peculiar six times lensed red galaxy appears in the cluster core. Four multiple images are located on the sides of the BCG, and other two tangential images are ∼16 arcsec northern and southern the BCG. Spectroscopic measurements of the images 1.1 and 1.5 place this galaxy at $z_{\rm sp} = 1.36$. In Fig. A1, the 1D and 2D spectra for images 1.1 and 1.5 are shown. The spectrum of this early-type galaxy shows a prominent 4000 Å break and no O[II] line in emission.

System 2. On the west side of the cluster, at a distance of ∼14 arcsec, a tangential arc and its counter image are found. The arc has a spectroscopic redshift of 1.04 with QF = 2. The spectrum for this system is shown in Fig. A1

System 3. At larger distance on the west side, there is a second long arc with respective counter image, which have likely spectroscopic redshift $z_{\rm sp} = 2.24$ (QF = 2). In Fig. A2, we show the 1D and 2D spectra for images 3.1 and 3.3.

System 4. A faint triply lensed source is identified on the eastern side of the cluster, at a distance of ∼30 arcsec. The three multiple images are clearly identified being composed of two bright knots. The image 4.3 was targeted with VIMOS, providing a likely source redshift of 2.24 (QF = 2), see Fig. A2.

System 5. This is a triply lensed system lying on the east side of the cluster core, at a distance of ∼20 arcsec from the BCG. Photometric redshift estimate place this lensed galaxy at $z_{\rm ph} \sim 1.5$–2.

System 6. This system is composed of three optical dropouts with photometric redshift $z_{\rm ph} \sim 6.5$. Huang et al. (2016) have recently published the spectroscopic confirmation for this system using Keck/DEIMOS (DEep Imaging Multi-Object Spectrograph) and *HST*/WFC3/G102 grism data. A clear Lyman α emission line places this triply imaged system at $z_{\rm sp} = 6.85$.

System 7. This system is another triply lensed galaxy that has photometric redshift estimation of $z_{\rm ph} \sim 1.4$.

In Fig. A3 in Appendix A, we show the optical and IR colour cut-out for the systems 5, 6 and 7, with their respective SED fit and photometric redshift, as available from the public CLASH archive (see footnote 2).

System 8. This is a candidate quadruply lensed source at $z_{\rm sp} = 4.4$. Image 8.1 was serendipitously discovered in the vicinity of a cluster member targeted with our VIMOS observations. We obtained a spectroscopic redshift of $z_{\rm sp} = 4.4$, based on a single emission line, identified as Lyman α (see Fig. A4). We photometrically identified three possible counter images of image 8.1 in the *HST* imaging that are supported by our lensing model, and are thus included in the model itself as constraints.

All the systems are summarized in Table 3. In total, we have 31 multiple images that provide constraints on our lensing model. We adopt uncertainties of 1 arcsec on the position of all the multiple images (except for system 1, see Section 4 for details), to take into account lens substructures and line-of-sight structures not considered in our model, which may introduce an offset of 0.5–2.5 arcsec on multiple images prediction (Jullo et al. 2010; Host 2012).

4 STRONG LENSING ANALYSIS

Given the mass components and the multiple images systems presented in the previous section, we perform the SL analysis of MACS 2129 by minimizing the distance between the observed and predicted multiple images. This is performed through a standard χ^2 minimization, where the χ^2 is defined as

$$\chi^2_{\rm tot} = \sum \left(\frac{|\boldsymbol{\theta}_i^{\rm pred} - \boldsymbol{\theta}_i^{\rm obs}|}{\sigma_i^{\rm pos}} \right)^2 , \quad (7)$$

where $\boldsymbol{\theta}_i{}^{\rm pred}$ is the predicted position of the ith multiple image, $\boldsymbol{\theta}_i^{\rm obs}$ is the observed multiple image position and $\sigma_i^{\rm pos}$ is its uncertainty.

[2] Available at http://archive.stsci.edu/prepds/clash/

Downloaded from https://academic.oup.com/mnras/article/466/4/4094/2869856 by guest on 19 November 2020

Table 3. Summary of the multiple images identified in the core of MACS 2129. Column 1: ID; columns 2 and 3: RA and Dec. in degrees; column 4: source redshift. Columns 5 and 6 give the redshift of the lensed sources and the offset $\delta\theta$ between the observed and predicted multiple images as derived from our SL model, see Section 5. All the systems have spectroscopic measurements, except for systems 5 and 7, for which we provide the photometric redshift measurements from the online public CLASH archive, with their 68 per cent ranges.

ID	RA	Dec.	z_s	z_{sl}	$\delta\theta$(arcsec)
1.1	322.357 97	−7.685 88	1.36	1.36	0.3
1.2	322.359 65	−7.690 82	”	”	0.2
1.3	322.359 25	−7.690 95	”	”	0.1
1.4	322.357 12	−7.691 09	”	”	0.2
1.5	322.357 64	−7.691 15	”	”	0.4
1.6	322.358 61	−7.694 89	”	”	0.6
2.1	322.354 83	−7.6907	1.04	1.04	0.2
2.2	322.354 77	−7.6916	”	”	0.1
2.3	322.355 38	−7.693 32	”	”	0.4
3.1	322.350 22	−7.688 86	2.24	2.24	1.8
3.2	322.350 04	−7.689 82	”	”	0.3
3.3	322.350 95	−7.695 77	”	”	1.7
4.1a	322.366 42	−7.686 74	2.24	”	0.4
4.1b	322.366 51	−7.686 89	”	”	0.3
4.2a	322.366 93	−7.688 31	”	”	0.4
4.2b	322.366 95	−7.688 20	”	”	0.2
4.3a	322.366 79	−7.694 97	”	”	0.3
4.3b	322.366 66	−7.695 25	”	”	1.3
5.1	322.364 22	−7.693 87	1.8 [1.4, 2.0]	1.71 ± 0.06	0.6
5.2	322.364 60	−7.691 37	2.0 [1.8, 2.3]	”	0.3
5.3	322.362 43	−7.684 93	1.8 [1.4, 2.2]	”	0.5
6.1	322.350 94	−7.693 33	6.85	6.85	1.4
6.2	322.353 24	−7.697 44	”	”	1.7
6.3	322.353 94	−7.681 64	”	”	1.9
7.1	322.357 14	−7.694 25	1.4 [1.2, 1.5]	1.33 ± 0.05	0.4
7.2	322.356 25	−7.691 72	–	”	0.7
7.3	322.356 70	−7.685 54	1.4 [1.1, 1.5]	”	0.5
8.1	322.356 98	−7.689 24	4.41	4.41	0.5
8.2	322.361 67	−7.688 08	”	”	1.4
8.3	322.358 60	−7.684 91	”	”	1.2
8.4	322.360 35	−7.700 94	”	”	1.4

We carry out the SL modelling through subsequent iterations, in which we include step by step the lensed systems in the model.

First, we perform the minimization analysis using as constraints only the two inner multiple systems with measured spectroscopic redshift (systems 1 and 2). Through this preliminary modelling, we keep fixed the b/a and PA of the BCG, G1 and G2. The position angle and axial ratio of these three galaxies are fixed to the values extracted with SExtractor in the filter $F814W$. The two lensed systems 1 and 2 provide 18 constraints through the positions of the respective multiple images. The free parameters are 18 in total: 6 for the DH, 2 for each of the individually optimized galaxy (GR, BCG, G1 and G2) and 4 for the x- and y-position of the lensed sources. Once we reach a preliminary model with good prediction for the multiple images, we add the outer spectroscopically confirmed systems 3, 4a and 4b. This increases the number of constraints to 36, while the free parameters are 24. The inclusion of these outer multiple images affects the accuracy in reproducing the central system 1: the minimization is mainly driven by the tangential multiple images of systems 2, 3 and 4, which place constraints on the large-scale DH, to the detriment of the central radial images of system 1. In order to improve the mass model in the very inner region, we reduce the positional error of system 1 to $\sigma^{\rm pos}_{\rm sys1} = 0.5$ arcsec, which gives a higher weight to this system in the $\chi^2_{\rm tot}$ minimization. As a result of this approach, we reach preliminary good prediction for all the spectroscopic confirmed systems, with $\chi^2 = 16.9/12$ dof and median rms 0.5 arcsec. In the next step, we include the multiple systems 5 to 8 with subsequent iterations and repeat the χ^2 minimization. The source redshift for systems 5 and 7 is unknown; thus, we use their photometric redshift as starting value, and optimize them using a Gaussian prior with width given by their respective $z_{\rm ph}$ uncertainties. At this stage, we release the b/a and PA of BCG, G1 and G2 and optimize within the range described in the previous section. In addition, we also allow the core radii of these three galaxies to vary within [0,3.5] kpc. The total number of degrees of freedom is 27, having finally 62 constraints and 41 free parameters. Besides the minimization analysis, we run MCMC chains to obtain the model that reproduces with best accuracy the observed multiple images and the uncertainties on our free parameters, i.e. the mass component parameters and the source redshift for systems 5 and 7.

5 RESULTS AND DISCUSSION

After the minimization and MCMC analyses, our final best mass model of the cluster has $\chi^2_{\rm tot} = 29$ having 21 degrees of freedom. It reproduces the multiple images with a median accuracy of 0.4 arcsec. In Fig. 3, we show the histogram of the offsets $\delta\theta$ between the

Downloaded from https://academic.oup.com/mnras/article/466/4/4094/2869856 by guest on 19 November 2020

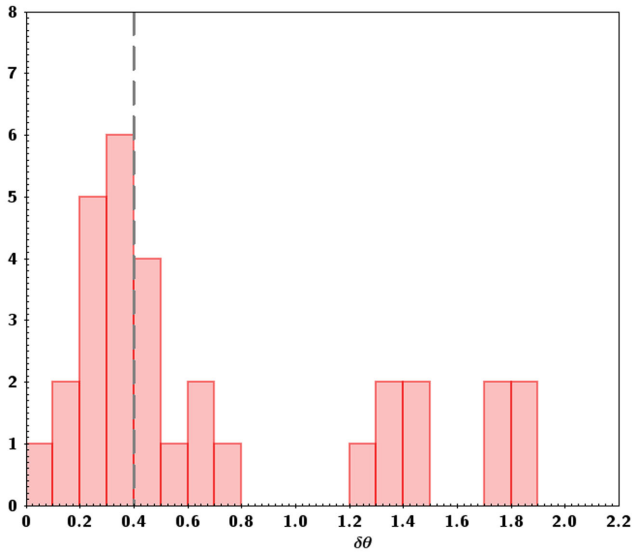

Figure 3. Histogram of the offsets $\delta\theta$ between the observed position of the multiple images and the predicted ones from our best SL model. Units are arcseconds. The vertical dashed line marks the median value of $\delta\theta$.

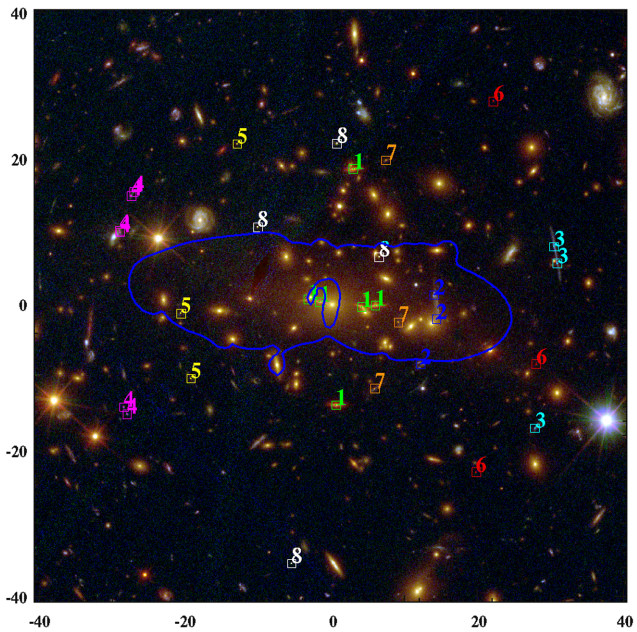

Figure 4. RGB colour composite image of MACS 2129 with the overplotted critical lines (in blue) for a source at the redshift $z_s = 1.36$. The multiple images used to constrain the cluster mass profile are labelled with squares in different colours (see Table A1). The axes are in arcseconds with respect to the BCG position.

observed and predicted images, which are listed in Table 3. In the inner region, inside the Einstein parameter of the cluster, the lensed systems 1, 2, 5 and 7 are reproduced with high accuracy, having median $\delta\theta = 0.4$ arcsec. Only the central system 8, which is a candidate quadruply lensed galaxy, has median $\delta\theta = 1.3$ arcsec. The image 8.1, which is spectroscopically confirmed at redshift $z_{\rm sp} = 4.4$, is reproduced with a small offset of 0.5 arcsec, whereas the three candidate counter images, photometrically selected, are predicted with accuracy of 1.3 arcsec. At larger radii ($r \gtrsim 30$ arcsec), we find that the two systems on the west of the cluster (systems 3 and 6) are reproduced with median $\delta\theta = 1.7$ arcsec, while on the east side, system 4 is reproduced with high accuracy of 0.4 arcsec. Based on the symmetry of the model (see Fig. 4), we can exclude that the particular shallowness of the DH profile is affecting the lensing prediction at large radii. Indeed, if this is the case, we would expect large $\delta\theta$ also for system 4. Thus, we conclude that the larger offset $\delta\theta = 1.7$ arcsec for the prediction of systems 3 and 6 is likely related to lens substructures or density inhomogeneities along the line of sight, which are not taken into account in our mass model. However, our photometric data set does not reveal any apparent intervening structure in this region.

In Table 4, we provide the final values obtained for the cluster mass component parameters.

The cluster DH has central position very close to the BGC, with $x_{\rm DH} = -2.0 \pm 0.7$ arcsec and $y_{\rm DH} = 1.5 \pm 0.3$ arcsec with respect to the BCG. It is highly elongated along the WE direction, with axial ratio $b/a = 0.32 \pm 0.03$ and position angle PA $= -7^\circ \pm 1^\circ$, measured anticlockwise from the west direction. The Einstein parameter is $\Theta_{\rm E} = 29 \pm 4$ arcsec, which corresponds to an Einstein radius of $\theta_{\rm E,sys1} = 14 \pm 2$ arcsec for a source at the redshift of system 1,$z_{\rm sys1} = 1.36$. The DH has a quite large core radius of $r_{\rm c} = 101^{+13}_{-11}$ kpc. Prediction of large DH core radii for galaxy clusters is not an unusual result in strong lensing analyses (see e.g. Richard et al. 2010b; Jauzac et al. 2014, 2015; Johnson et al. 2014; Grillo et al. 2015). In the innermost region of the cluster, lensing probes the total mass of the cluster core. This is given by the superposition of the PIEMD profile describing the large-scale DH and the dPIE profile that describes the baryonic mass component of the BCG. Obviously, the core of the large-scale DH profile correlates with the baryonic mass distribution of the BCG. The amplitude of the BCG stellar mass profile is described by a *central velocity dispersion* $\sigma^{\rm dPIE}_{0,\rm BCG}$ parameter, for the dPIE profile. This does not correspond to the spectroscopic measured central stellar velocity dispersion of the galaxy $\sigma^*_{\rm sp}$, since in this case $\sigma^{\rm dPIE}_{0,\rm BCG}$ simply provide an estimate of the mass amplitude of the BCG stellar component, and is not related to the dynamical velocity dispersion of the galaxy. This can be seen in Newman et al. (2013a,b) where, by combining lensing and kinematic analyses, they derive the amplitude $\sigma^{\rm dPIE}_{0,\rm BCG}$ of the BCG stellar mass profile for several galaxy clusters, and the results indeed depart from the spectroscopic measurement of the central velocity dispersion of the BCGs. For example, for the BCG of Abell 611 they get $\sigma^{\rm dPIE}_{0,\rm BCG} = 164 \pm 33\,{\rm km\,s^{-1}}$ for the baryonic dPIE profile, whereas the spectroscopic measurement of the central velocity dispersion provides $\sigma^*_{\rm BCG,sp} = 317 \pm 20\,{\rm km\,s^{-1}}$. Sand et al. (2002, 2004) and Newman et al. (2013a,b) show the utility to combine the BCG stellar kinematic analysis with strong lensing to disentangle the DH and the stellar mass components in the innermost region of galaxy clusters. Newman et al. (2013b) separate the baryonic and DM components in seven galaxy clusters. They find that the size and mass of the BCG correlate with the core radii of the DH mass profile, and that larger BCGs are hosted by clusters with larger core radii. However, they obtain typical DH core radii $r_{\rm c} \approx 10$–20 kpc for the clusters of their sample. Thus, the large core radius resulting in our analysis may reflect an overestimate of the mass associated with the BCG component. Indeed, from our analysis, we get $\sigma^{\rm dPIE}_{0,\rm BCG} = 370 \pm 25\,{\rm km\,s^{-1}}$ as amplitude of the BCG stellar mass profile, which is rather high when compared to the results from Newman et al. (2013a,b) for the BCG stellar profiles. In order to properly disentangle the large-scale DH and the BCG baryonic mass components in the core of the cluster, the lensing analysis

Downloaded from https://academic.oup.com/mnras/article/466/4/4094/2869856 by guest on 19 November 2020

Table 4. Final parameters of the mass components of MACS 2129 with their respective 1σ uncertainty. The DH position (x, y) is given in arcseconds with respect to the BCG. The core and truncation radii are in kpc, velocity dispersions are in km s^{-1} and PA are in degrees measured anticlockwise from the west direction.

DH	
x	-2.0 ± 0.7
y	1.5 ± 0.3
b/a	0.32 ± 0.03
PA	-7 ± 1
$\Theta_{\rm E}$(arcsec)	29 ± 4
$r_{\rm c}$	101^{+13}_{-11}
GR	
σ_0	185^{+20}_{-16}
$r_{\rm tr}$	66^{+22}_{-28}
BCG	
b/a	0.78 ± 0.10
PA	2.5 ± 2.8
σ_0	370 ± 25
$r_{\rm c}$	$1.1^{+1.2}_{-0.8}$
$r_{\rm tr}$	87^{+32}_{-35}
G1	
b/a	0.86 ± 0.05
PA	54 ± 3
σ_0	224^{+52}_{-38}
$r_{\rm c}$	$1.6^{+1.1}_{-1.0}$
$r_{\rm tr}$	57^{+30}_{-37}
G2	
b/a	0.80 ± 0.05
PA	130 ± 3
σ_0	255 ± 28
$r_{\rm c}$	$1.3^{+1.3}_{-1.0}$
$r_{\rm tr}$	25^{+28}_{-21}

alone is not enough, and additional constraints, as kinematics, are needed. In Fig. 5, we plot the DH core radius versus the dPIE velocity dispersion of the BCG stellar mass profile for our mass model to show the correlation between these two parameters. In Fig. 6, we also show the mass profile for both these mass components. Given the total mass profile of the cluster robustly probed by the lensing analysis, we can see that a higher BCG stellar mass profile would imply a shallower profile for the DH, i.e. a larger DH core. In addition, we verified that, if we did not use a separate mass profile to describe the BCG and the innermost cluster mass would have been modelled by a PIEMD profile alone, then we would obtain a cluster core radius as small as $\approx$5 kpc, which places a lower limit to the DH core.

Given our final best model of the cluster, we extract the projected mass of the different cluster components within the Einstein parameter. The projected mass of the large-scale DH is constrained with 8 per cent precision, with $M_{\rm DH} = (8.6 \pm 0.6) \times 10^{13}\,{\rm M}_{\odot}$ within

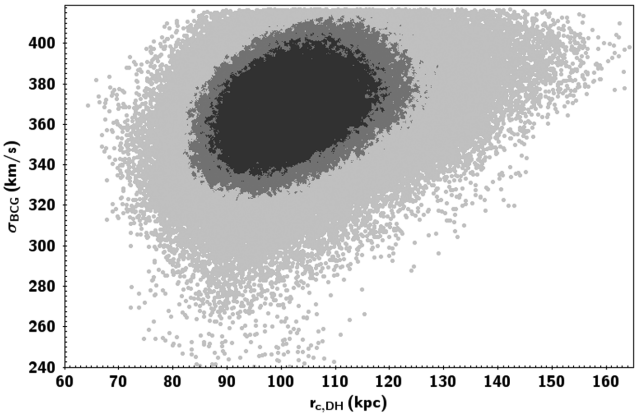

Figure 5. Large-scale DH core radius versus the velocity dispersion of the dPIE mass profile describing the cluster BCG. The grey-scale corresponds to the 1σ (black), 2σ (dark grey) and 3σ (light grey) confidence level region.

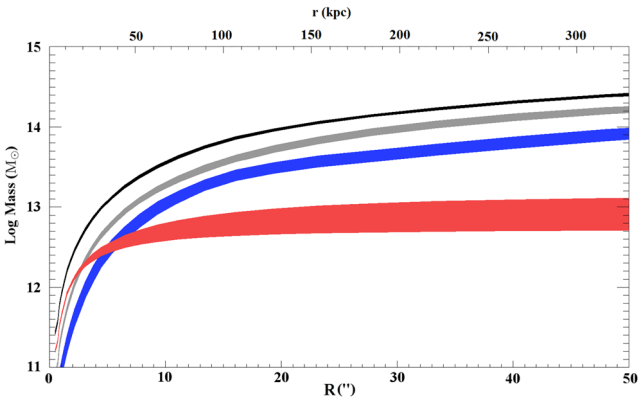

Figure 6. Projected 2D mass profile at 68 per cent confidence level of the core of MACS 2129. In red, we plot the BCG stellar mass profile, in blue we plot the total mass of the other cluster members, in grey the cluster DH and in black the total mass profile.

$\Theta_{\rm E} = 29 \pm 4$ arcsec. The BCG has a projected baryonic mass of $M_{\rm BCG}(< \Theta_{\rm E}) = (8.4 \pm 2) \times 10^{12}\,{\rm M}_{\odot}$.

The reference galaxy GR has central velocity dispersion $\sigma_{0,\rm GR} = 185^{+20}_{-16}$ km s^{-1} and truncation radius $r_{\rm tr,GR} = 66^{+22}_{-28}$ kpc, providing the following cluster scaling relation:

$$r_{\rm tr} = 66^{+22}_{-28}\,{\rm kpc}\left(\frac{\sigma}{185^{+20}_{-16}\,{\rm km\,s^{-1}}}\right)^{\frac{4}{3}}. \quad (8)$$

The other two galaxies individually optimized, G1 and G2, get velocity dispersion with 1σ errors of $\lesssim$20 per cent, but their truncation radii have very large uncertainties. The total projected mass of the other cluster galaxies is constrained at level of 12 per cent, with $M_{\rm gal} = (4.4 \pm 0.5) \times 10^{13}\,{\rm M}_{\odot}$ within the Einstein parameter $\Theta_{\rm E}$.

Overall the joint projected cluster mass of the large-scale DH, BCG and the galaxy component is $M_{\rm tot}(< \Theta_{\rm E}) = (1.35 \pm 0.03) \times 10^{14}\,{\rm M}_{\odot}$, and it is constrained with 2 per cent precision. In Fig. 6, we show the 2D projected mass profiles of the DH, BCG, the galaxy component and the total mass of the cluster core up to a radial distance of 50 arcsec from the cluster centre.

Downloaded from https://academic.oup.com/mnras/article/466/4/4094/2869856 by guest on 19 November 2020

Zitrin et al. (2015) published a first model of MACS 2129 using the CLASH data set. They obtain a total projected mass of $M_e = (9.2 \pm 0.9) \times 10^{13}\,\mathrm{M}_\odot$ within the Einstein radius $\theta_\mathrm{E} = 19 \pm 2$ arcsec for a source at redshift $z_\mathrm{s} = 2$. Within the same radius, we extract a total mass of $M_\mathrm{tot}(<19\,\mathrm{arcsec}) = (8.9 \pm 0.1) \times 10^{13}\,\mathrm{M}_\odot$, which is fully consistent with the previous analysis from Zitrin et al. (2015). We highlight that the larger uncertainties in Zitrin et al. (2015) account also for systematics, derived by modelling the DH cluster with different analytic mass profiles.

6 SUMMARY AND CONCLUSIONS

In this paper, we presented a precise strong lensing analysis of the massive cluster of galaxies MACS 2129. We combine the CLASH high-resolution photometry with the new VLT spectroscopy from the CLASH-VLT surveys to robustly select cluster members and multiple images needed for the SL modelling. This cluster shows a peculiar sextuply lensed red passive galaxy in its core, which has spectroscopic redshift $z_\mathrm{sp} = 1.36$. Six additional multiple lensed sources are clearly identified in the cluster core. Our CLASH-VLT spectroscopic data provide spectroscopic redshift confirmation for three of these lensed systems. We use these multiple images to constrain the mass profile in the innermost region of the cluster with very high precision. Our best mass reconstruction of the cluster reproduces the observed multiple images with a median accuracy of 0.4 arcsec. The overall high accuracy in predicting the position of the multiple images directly translates to a high-precision reconstruction of the total mass distribution of the cluster.

The cluster DH projected mass is constrained with 8 per cent precision, with $M_\mathrm{DH} = (8.6 \pm 0.6) \times 10^{13}\,\mathrm{M}_\odot$ within the Einstein parameter $\Theta_\mathrm{E} = 29 \pm 4$ arcsec. The DH has a large core radius $r_\mathrm{c} = 101^{+13}_{-11}$ kpc, similar to other galaxy cluster (Richard et al. 2010a; Jauzac et al. 2014, 2015; Johnson et al. 2014; Grillo et al. 2015). However, the DH core radius correlates with the BCG mass profile. When the BCG baryonic and the cluster DH components are properly disentangled by combining lensing and kinematic analyses, typical smaller core radii ($r_\mathrm{c} \approx 10$–20 kpc) are found for cluster DHs (see Newman et al. 2013a,b). Thus, the large core radius we derived likely reflects an overestimate of the mass associated with the BCG mass component. Nevertheless, the final 2D projected total mass of the cluster is constrained with an accuracy of 2 per cent. Within the Einstein parameter, it is $M_\mathrm{tot} = (1.35 \pm 0.03) \times 10^{14}\,\mathrm{M}_\odot$.

In addition to the mass model for the core of MACS 2129, we also provide the complete list of robust spectroscopic redshifts of cluster members and lensed features measured with VLT/VIMOS within the CLASH-VLT survey, see Appendix A.

ACKNOWLEDGEMENTS

This work is supported by the Transregional Collaborative Research Centre TRR 33 – The Dark Universe and the DFG cluster of excellence 'Origin and Structure of the Universe'. The CLASH Multi-Cycle Treasury Program (GO-12065) is based on observations made with the NASA/ESA *Hubble Space Telescope*. The Space Telescope Science Institute is operated by the Association of Universities for Research in Astronomy, Inc. under NASA contract NAS5-26555. SHS gratefully acknowledges support from the Max Planck Society through the Max Planck Research Group. PR and AMe acknowledge support from PRIN-INAF 2014 1.05.01.94.02 (PI: M. Nonino). PR acknowledges the hospitality and support of the visitor programme of the DFG cluster of excellence 'Origin and Structure of the Universe'. CG acknowledges support by VILLUM FONDEN Young Investigator Programme through grant no. 10123.

REFERENCES

Arnouts S., Cristiani S., Moscardini L., Matarrese S., Lucchin F., Fontana A., Giallongo E., 1999, MNRAS, 310, 540
Balestra I. et al., 2016, ApJS, 224, 33
Bertin E., Arnouts S., 1996, A&AS, 117, 393
Biviano A. et al., 2013, A&A, 558, A1
Calzetti D., Armus L., Bohlin R. C., Kinney A. L., Koornneef J., Storchi-Bergmann T., 2000, ApJ, 533, 682
Coe D. et al., 2012, ApJ, 757, 22
Donahue M. et al., 2014, ApJ, 794, 136
Ebeling H., Barrett E., Donovan D., Ma C.-J., Edge A. C., van Speybroeck L., 2007, ApJ, 661, L33 (MACS 2129)
Eichner T. et al., 2013, ApJ, 774, 124
Elíasdóttir Á. et al., 2007, preprint (arXiv:0710.5636)
Grillo C. et al., 2015, ApJ, 800, 38
Host O., 2012, MNRAS, 420, L18
Huang K.-H. et al., 2016, ApJ, 823, L14
Ilbert O. et al., 2006, A&A, 457, 841
Ilbert O. et al., 2009, ApJ, 690, 1236
Jauzac M. et al., 2014, MNRAS, 443, 1549
Jauzac M. et al., 2015, MNRAS, 452, 1437
Johnson T. L., Sharon K., Bayliss M. B., Gladders M. D., Coe D., Ebeling H., 2014, ApJ, 797, 48
Jullo E., Natarajan P., Kneib J.-P., D'Aloisio A., Limousin M., Richard J., Schimd C., 2010, Science, 329, 924
Kassiola A., Kovner I., 1993, in Surdej J., Fraipont-Caro D., Gosset E., Refsdal S., Remy M., eds, Gravitational Lenses in the Universe, Proceedings of the 31st Liege International Astrophysical Colloquium (LIAC 93). Universite de Liege/Institut d'Astrophysique, Liege, p. 571
Koekemoer A. M. et al., 2011, ApJS, 197, 36
Le Fèvre O. et al., 2003, in Iye M., Moorwood A. F. M., eds, Proc. SPIE Vol. 4841, Instrument Design and Performance for Optical/Infrared Ground-based Telescopes. SPIE, Bellingham, p. 1670
Medezinski E. et al., 2013, ApJ, 777, 43
Monna A. et al., 2015, MNRAS, 447, 1224
Newman A. B., Treu T., Ellis R. S., Sand D. J., Richard J., Marshall P. J., Capak P., Miyazaki S., 2009, ApJ, 706, 1078
Newman A. B., Treu T., Ellis R. S., Sand D. J., 2011, ApJ, 728, L39
Newman A. B., Treu T., Ellis R. S., Sand D. J., Nipoti C., Richard J., Jullo E., 2013a, ApJ, 765, 24
Newman A. B., Treu T., Ellis R. S., Sand D. J., 2013b, ApJ, 765, 25
Postman M. et al., 2012, ApJS, 199, 25
Prevot M. L., Lequeux J., Prevot L., Maurice E., Rocca-Volmerange B., 1984, A&A, 132, 389
Richard J., Kneib J.-P., Limousin M., Edge A., Jullo E., 2010a, MNRAS, 402, L44
Richard J. et al., 2010b, MNRAS, 404, 325
Rosati P. et al., 2014, Messenger, 158, 48
Sand D. J., Treu T., Ellis R. S., 2002, ApJ, 574, L129
Sand D. J., Treu T., Smith G. P., Ellis R. S., 2004, ApJ, 604, 88
Scodeggio M. et al., 2005, PASP, 117, 1284
Stern D., Jimenez R., Verde L., Stanford S. A., Kamionkowski M., 2010, ApJS, 188, 280
Suyu S. H., Halkola A., 2010, A&A, 524, A94
Suyu S. H. et al., 2012, ApJ, 750, 10
Treu T. et al., 2015, ApJ, 812, 114
Umetsu K. et al., 2012, ApJ, 755, 56

Downloaded from https://academic.oup.com/mnras/article/466/4/4094/2869856 by guest on 19 November 2020

Umetsu K., Zitrin A., Gruen D., Merten J., Donahue M., Postman M., 2016, ApJ, 821, 116
Zitrin A., Broadhurst T., Barkana R., Rephaeli Y., Benítez N., 2011, MNRAS, 410, 1939
Zitrin A. et al., 2015, ApJ, 801, 44

APPENDIX A: CLUSTER MEMBERS AND LENSED IMAGES SPECTROSCOPY

In this appendix, we provide the spectroscopic information from the CLASH-VLT survey for all the confirmed cluster members (in Table A2) as well as the list of all the lensed sources targeted with VLT, including the multiple images systems 1 to 4 and system 8, used in the strong lensing analysis (see Table A1).

We remark that only two slit masks were used with the VIMOS MR grism due to strong galactic cirrus in MACS 2129, resulting in a small number of redshifts compared to other CLASH-VLT clusters.

Table A1. List of the spectroscopically confirmed lensing features in the core of MACS 2129. Column 1: ID; columns 2 and 3: RA and Dec. in degrees; column 4: spectroscopic redshift; column 5: quality flag. The first six objects are multiple images used in the strong lensing model.

ID	RA	Dec.	z_{sp}	QF
1.1	322.358 001	−7.685 835	1.3649	2
1.5	322.357 147	−7.691 137	1.3641	3
2.1	322.354 838	−7.690 73	1.0400	2
3.1	322.350 27	−7.688 832	2.2362	2
3.3	322.350 971	−7.695 714	2.2392	2
4.1	322.366 451	−7.686 847	2.2367	2
8	322.356 98	−7.689 239	4.4107	9
9	322.363 02	−7.685 172	1.4519	9
10	322.368 227	−7.692 496	1.5453	3
11	322.361 659	−7.696 394	0.9484	3
12	322.354 701	−7.700 377	2.4129	2
13	322.348 531	−7.699 152	0.9474	3
14	322.362 804	−7.683 168	2.3082	2
15	322.340 94	−7.684 378	2.2707	3
16	322.360 655	−7.704 58	1.9939	2
17	322.354 359	−7.705 515	1.1815	3
18	322.355 495	−7.707 085	1.0511	3
19	322.370 793	−7.709 214	1.0495	3
20	322.350 806	−7.681 908	1.3599	3
21	322.364 81	−7.683 756	1.3698	3
22	322.362 883	−7.682 68	2.3082	2

Table A2. List of MACS 2129 cluster members spectroscopically confirmed by VLT/VIMOS data. Column 1: ID; columns 2 and 3: RA and Dec. in degrees; column 4: VIMOS spectroscopic redshift; column 5: quality flag.

ID	RA	Dec.	z_{sp}	QF
10481	322.189 736	−7.656 97	0.5887	3
10794	322.347 084	−7.663 556	0.5922	3
10916	322.365 14	−7.666 103	0.5937	3
10930	322.353 041	−7.666 496	0.5942	3
11120	322.327 031	−7.670 48	0.5927	3
11141	322.337 188	−7.670 573	0.5959	3
11422	322.311 935	−7.676 886	0.5865	3
11760	322.340 785	−7.683 884	0.5817	2
12388	322.357 097	−7.689 107	0.5833	3
12431	322.201 623	−7.696 05	0.5948	3
12475	322.350 967	−7.697 143	0.5933	3
12489	322.245 821	−7.697 805	0.5835	3
12490	322.245 601	−7.698 231	0.5807	3
13051	322.353 276	−7.707 495	0.5746	3
13052	322.353 245	−7.707 943	0.5904	3
13061	322.290 916	−7.707 586	0.5961	3
13217	322.333 338	−7.710 552	0.5928	3
13373	322.325 793	−7.714 155	0.5832	3
13652	322.360 905	−7.719 659	0.5886	2
13694	322.316 236	−7.720 489	0.578	3
13886	322.350 413	−7.724 35	0.5738	2
14049	322.394 194	−7.728 681	0.5779	3
14147	322.402 022	−7.729 684	0.5999	3
14698	322.303 043	−7.741 079	0.5906	3
14851	322.145 996	−7.744 111	0.5868	3
16408	322.343 14	−7.782 107	0.5901	3
17053	322.211 216	−7.795 855	0.5894	2
17545	322.321 102	−7.806 902	0.5788	3
17758	322.192 709	−7.811 686	0.5934	3
4248	322.165 238	−7.892 864	0.5851	3
4351	322.311 384	−7.890 688	0.5854	3
4506	322.151 681	−7.887 87	0.5952	3
4518	322.151 734	−7.886 972	0.5955	3
4588	322.139 294	−7.886 331	0.5814	3
5525	322.169 704	−7.863 769	0.5737	3
5652	322.304 068	−7.860 543	0.5869	3
6351	322.227 851	−7.845 947	0.5764	3
6485	322.298 203	−7.843 324	0.5809	3
6529	322.210 264	−7.842 364	0.5858	3
6558	322.362 822	−7.842 443	0.5777	3
6830	322.322 366	−7.835 512	0.5875	3
7255	322.222 26	−7.824 324	0.5744	2
7359	322.189 632	−7.822 517	0.5947	3
9492	322.228 274	−7.634 417	0.5834	3
9744	322.342 228	−7.639 917	0.5841	3
13198	322.207 45	−7.710 083	0.5843	2
5448	322.208 39	−7.861 958	0.587 85	3
12133	322.354 958	−7.691 768	0.5959	3

Downloaded from https://academic.oup.com/mnras/article/466/4/4094/2869856 by guest on 19 November 2020

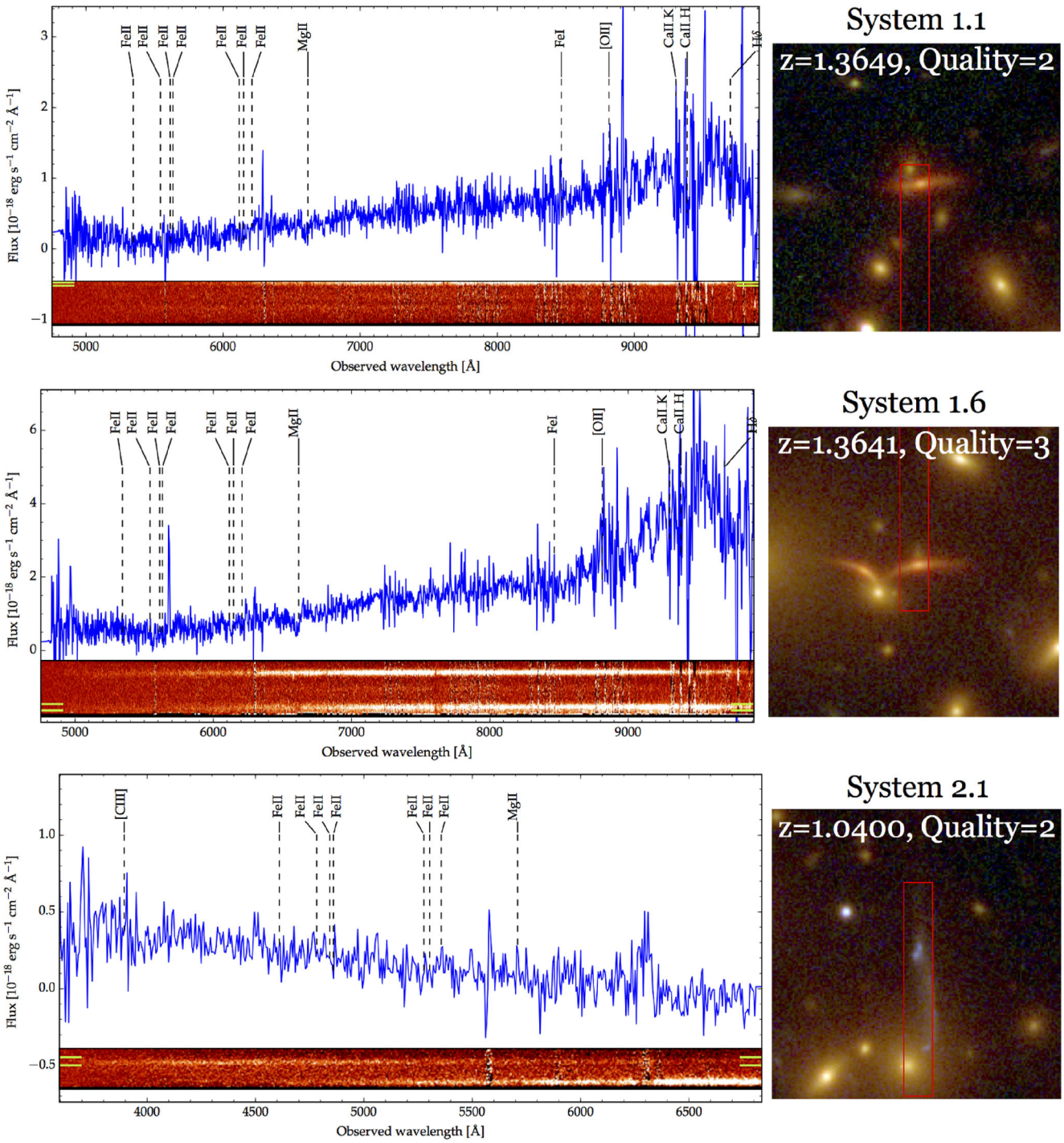

Figure A1. Spectroscopy of the multiple images of systems 1 and 2 observed with VLT/VIMOS. On the left, we present the 2D (lower panel) and 1D spectra (upper panel). The dashed vertical lines in the 1D spectra mark emission and absorption lines used to derive the source redshift. On the right, we show the *HST* colour composite image cut-out of the observed multiple image. The red rectangles mark the position of the 1-arcsec-long VIMOS slits. In the 2D spectra, we use two green lines to indicate the position of the emission associated with the lensed image.

Downloaded from https://academic.oup.com/mnras/article/466/4/4094/2869856 by guest on 19 November 2020

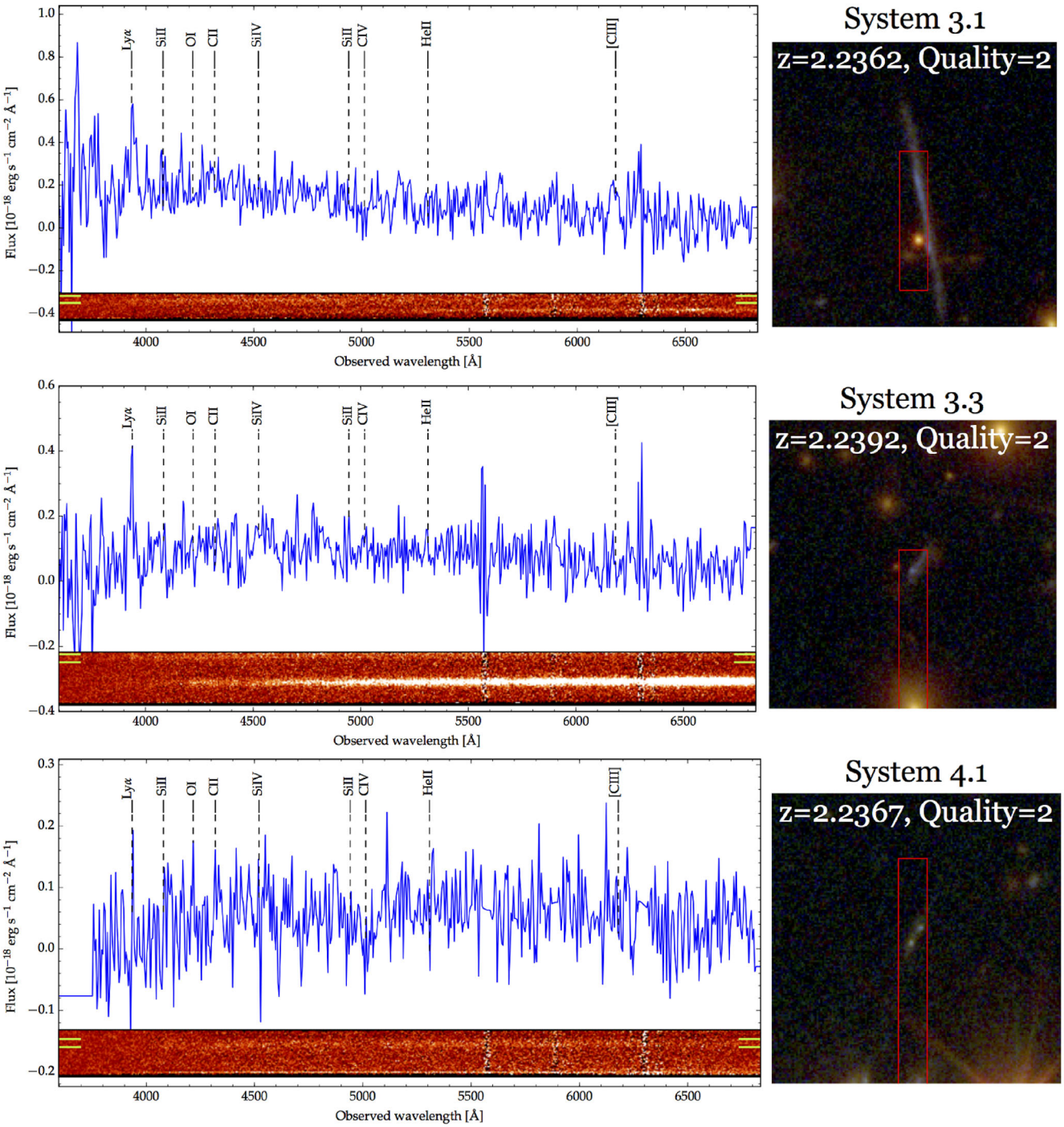

Figure A2. Same as Fig. A1, for the multiple images systems 3 and 4.

Downloaded from https://academic.oup.com/mnras/article/466/4/4094/2869856 by guest on 19 November 2020

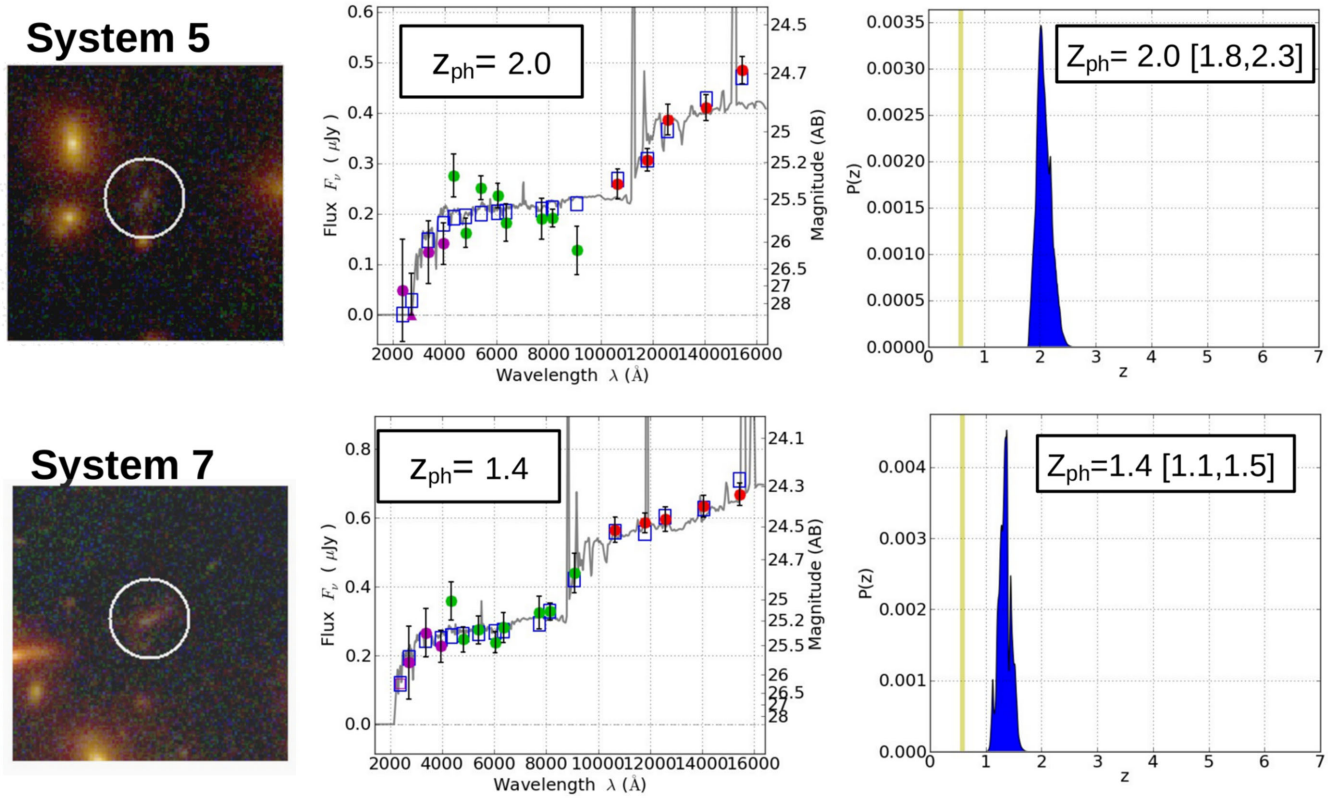

Figure A3. SED for the multiple images systems 5 and 7, derived using the CLASH photometry and the SED fit code BPZ. We present the fit of the multiple images 5.2 and 7.3, which get well-defined PDF(z). On the left, we show the lensed images cut-out in the colour composite image of the cluster. The white circle labels the image and has diameter of ∼1.5 arcsec. The central panel shows the SED fitted with the photometric measurement from CLASH, showing in violet the fluxes in the WFC3UVIS filter, in green the one in the ACS and in red the IR photometry observed with the WFC3IR. The grey line shows the best template fitting the photometry, and in the legend we provide the respective best-fitting redshift. On the right, we show the respective PDF(z) and provide the best-fitting z_{ph} with the respective 68 per cent confidence level interval. The vertical yellow line marks the cluster redshift.

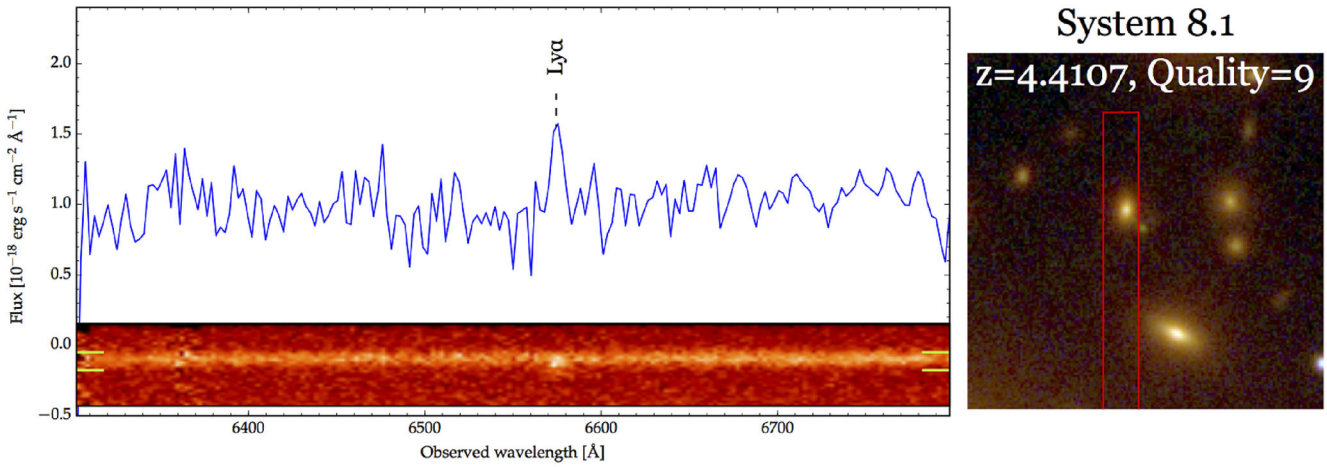

Figure A4. Same as Fig. A1 for the multiple lensed image 8.1 at redshift $z_{sp} = 4.4$. The lensed image is the green bright source lying close to the slit edge in the RGB cut-out.

This paper has been typeset from a TEX/LATEX file prepared by the author.

Downloaded from https://academic.oup.com/mnras/article/466/4/4094/2869856 by guest on 19 November 2020